Isotropic springs based on parallel flexure stages

L. Rubbert*, R. Bitterli, N. Ferrier, S. Fifanski, I. Vardi, S. Henein

Instant-Lab, École Polytechnique Fédérale de Lausanne, Neuchâtel, Switzerland

A B S T R A C T

We define *isotropic springs* to be central springs having the same restoring force in all directions. In previous work, we showed that isotropic springs can be advantageously applied to horological time bases since they can be used to eliminate the escapement mechanism [7]. This paper presents our designs based on planar serial 2-DOF linear isotropic springs. We propose two architectures, both based on parallel leaf springs, then evaluate their isotropy defect using firstly an analytic model, secondly finite element analysis and thirdly experimental data measured from physical prototypes. Using these results, we analyze the isotropy defect in terms of displacement, radial distance, angular separation, stiffness and linearity. Based on this analysis, we propose improved architectures stacking in parallel or in series duplicate copies of the original mechanisms rotated at specific angles to cancel isotropy defect. We show that using the mechanisms in pairs reduces isotropy defect by one to two orders of magnitude.

© 2015 The Authors. Published by Elsevier Inc. This is an open access article under the CC BY-NC-ND license (http://creativecommons.org/licenses/by-nc-nd/4.0/).

1. Introduction

The biggest improvement in timekeeper accuracy was due to the introduction of the oscillator as a time base, first the pendulum by Christiaan Huygens in 1656 [10], then the balance wheel–spiral spring by Huygens and Hooke in about 1675, and the tuning fork by Niaudet and Breguet in 1866 [14]. Since that time, these have been the only mechanical oscillators used in mechanical clocks and in all watches.

In [7], we presented new time bases for mechanical timekeepers which, in their simplest form, were based on a harmonic oscillator first described in 1687 by Isaac Newton in *Principia Mathematica* [13, Book I, Proposition X]. This oscillator is the isotropic harmonic oscillator, where a mass m at position $\boldsymbol{r}$ is subject to a central linear (Hooke) force.

Since the resulting trajectories have unidirectional rotation, this oscillator has the advantage of solving the problem of inefficiency of the escapement by eliminating it or, alternatively, simplifying it [7]. Isochronism is the key feature of a good time base, and in this case, the spring of the spring–mass system must be as isotropic as possible, meaning that in every direction, the spring stiffness and mass must remain the same. In addition, it should be planar in order to be easy to manufacture at any scale (note that Newton's model implies planar motion, by preservation of angular momentum).

In this paper, we mechanize Newton's model by designing new planar isotropic springs. Our designs are based on the principle of *compliant XY-stages* [1,3,11,12] which are mechanism with two degrees of freedom (2-DOF) both of which are translations. As these mechanisms are composed of compliant joints [9] they exhibit planar restoring forces so can be considered as planar springs. In the literature, many planar flexible *XY*-stages have been proposed and if some may be implicitly isotropic, none has been explicitly declared to be isotropic. This could be explained by the fact that, in general, *XY*-stages are controlled in closed-loops [17] and isotropy stiffness defects are therefore not necessarily a matter of concern. Moreover, we use a serial architecture instead of the parallel one generally seen in *XY*-stages used actuator integration applications.

Simon Henein [6, p. 156, 158] proposed two non-planar architecture *XY*-stages exhibiting planar isotropy. The first is composed of two serial compliant four-bar mechanisms, also called parallel arm linkage, which produce, for small displacements, translations in *X* and *Y* (see also [5]). The second is composed of four parallel arms linked by eight spherical joints and a bellow connecting the mobile platform to the ground.

In this paper the designs of two central springs based on parallel leaf springs are presented after a brief presentation of the context. For each of both designs, their analytical model is presented and compared to the performance based on finite element analysis and on experimental data of physically constructed prototypes.

Some images of these designs have appeared in [7] and some appear in recent patent applications.

* Corresponding author.
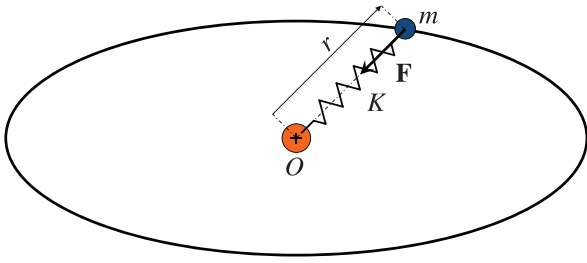 *E-mail address:* lennart.rubbert@insa-strasbourg.fr (L. Rubbert).

Fig. 1. Elliptical orbit under central Hooke Law.

2. Context

In order to understand the elliptical trajectories of planets predicted by Kepler's Laws, Isaac Newton considered the possible central laws producing elliptical orbits and he showed that apart from the inverse square law, a linear Hooke's law would also produce elliptical orbits,[1] see Fig. 1.

Newton's result is very easily shown. Consider a point mass moving in two dimensions subject to a central force

$$F(r) = -Kr,$$

where r is the distance of the mass to the center. Applying Newton's second law $F = ma$, where m is the mass of the particle and a its acceleration, gives the general solution

$$\mathbf{r} = (A_1 \sin(\omega_0 t + \varphi_1), A_2 \sin(\omega_0 t + \varphi_2)), \quad (1)$$

for initial conditions $A_1, A_2, \varphi_1, \varphi_2$ and frequency

$$\omega_0 = \sqrt{\frac{K}{m}}.$$

This shows that orbits are elliptical, but also that the period only depends on the mass m and the stiffness K of the central force, and not on the energy of the system, what is generally called *isochronism*. This last property is the key feature of horological time bases in which the regulation must be kept independent of the energy source. It follows that this oscillator is a good candidate to be a time base for a timekeeper, an observation first made in our previous article [7].

In order to exploit this oscillator as a mechanical time base, Newton's model must be followed as closely as possible. In particular, the mechanism's central linear restoring force must be as isotropic as possible. Expressed quantitatively, the isotropy defect must be minimized.

3. Definition of isotropy defect

The first step in analyzing the isotropy defect of a central spring is to give a precise definition of what is meant by *isotropy defect*. In particular, since isotropy defect only applies to central springs, the term "central" will be suppressed without ambiguity. The basic context of our isotropy defect computations is given in Fig. 2.

3.1. Baseline behavior

In order to evaluate isotropy defect, a baseline is required for comparison. We assume that our spring has *ideal stiffness K*. A force $\mathbf{F}_\theta$ of magnitude F and direction θ is applied, where θ will vary between $0°$ and $360°$ and the magnitude F will be constant (i.e.
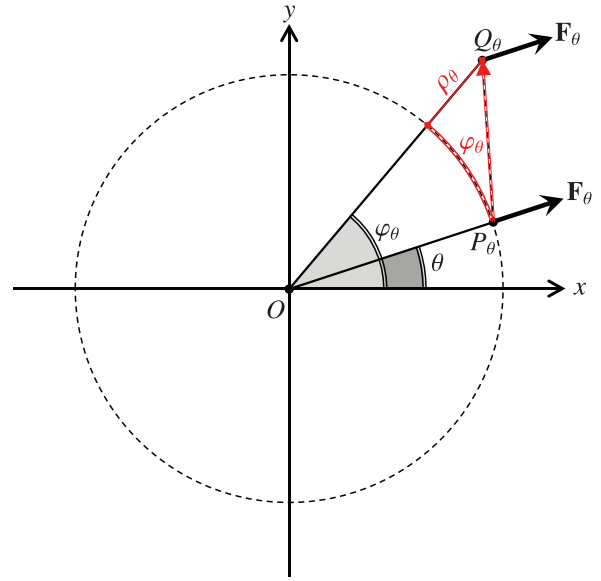

Fig. 2. Basic model of isotropy defect.

independent of θ). Under this force, the point O on the spring moves to the *ideal position* P_θ, and by Hooke's Law, $\vec{OP_\theta}$ has magnitude F/K and direction θ, see Fig. 2. Therefore, as θ varies between $0°$ and $360°$, the ideal point P_θ describes a perfect circle of radius F/K, and the restoring force is linear and isotropic.

3.2. Definitions

The previous example illustrates ideal behavior with zero isotropy defect. Divergence from this example will be used to measure the isotropy defect. Thus, when isotropy defect does occur, the force $\mathbf{F}$ will move the point O to a point Q_θ generally distinct from P_θ, see Fig. 2. The *isotropy defect vector* in the direction θ is defined to be $\vec{P_\theta Q_\theta}$.

In order to evaluate and compare the isotropy defect of our mechanisms, it is more convenient to have scalar measures of isotropy defect. We therefore define the simpler *radial isotropy defect* given by

$$\rho_\theta = \|\vec{OQ_\theta}\| - \|\vec{OP_\theta}\|.$$

Note that this measure of isotropy defect considers the discrepancy between the magnitudes of the actual displacement and the ideal displacement for angle θ which is different from the magnitude $\|\vec{P_\theta Q_\theta}\|$ of the isotropy defect vector, see Fig. 2.

The *angular isotropy defect* φ_θ is defined as the angle between $\vec{OP_\theta}$ and $\vec{OQ_\theta}$, as measured in the counterclockwise direction, see Fig. 2.

In order to define stiffness isotropy defect, we first introduce the notion of stiffness in a given direction θ by

$$k_\theta = \frac{F}{\|\vec{OP_\theta}\| + \rho_\theta} = \frac{F}{\|\vec{OQ_\theta}\|}.$$

The *stiffness isotropy defect* in the θ direction is then

$$\Delta k_\theta = K - k_\theta,$$

where K is the ideal stiffness defined as the maximum of k_θ for all angles. Note that Δk_θ is non-negative, by definition of K.

The *relative stiffness isotropy defect* in the θ direction is defined as

$$\eta_\theta = \frac{\Delta k_\theta}{k_\theta} = \frac{\rho_\theta}{\|\vec{OP_\theta}\|},$$

---

[1] The occurrence of ellipses in both laws is now understood to be due to a relatively simple mathematically equivalence [4] and it is also well-known that these two cases are the only central force laws leading to closed orbits [2,15].
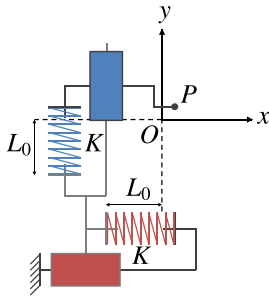
Fig. 3. Conceptual design of our isotropic springs.

where the right hand expression follows by applying $K = F/\|\vec{OP_\theta}\|$.

We finally define the *stiffness isotropy defect* to be $\eta_{\max}$, the maximum of η_θ over all $0° \leq \theta < 360°$. This will be used in Section 7 to evaluate isotropy performance.

In addition, we need our central springs to be linear, i.e., the relation between force and displacement should be linear. In order to evaluate this quantitatively, for each mechanism and for each force direction, a second order polynomial fit is applied to the displacement versus the force. Formally, this means that the force is written in polar coordinates r and θ as $\mathbf{F}_\theta = (A_\theta + B_\theta r + C_\theta r^2)\mathbf{u}_\theta$, with $\mathbf{u}_\theta$ a unit vector in the θ direction. For a linear spring $A_\theta = C_\theta = 0$ and B_θ defines the constant spring stiffness in the θ direction. Thus, C_θ quantifies the stiffness linearity defect.

Remark 3.2. In order to simplify notation, the subscript θ in these quantities may be suppressed in the following.

4. Isotropic spring design

Formula (1) of Section 2 shows that harmonic isotropic oscillator solutions can be considered as sums of two independent linear 1-DOF oscillators, one in the x direction and the other in the y direction. For this reason, we have chosen to consider planar isotropic springs following the conceptual configuration shown in Fig. 3. This configuration consists of two linear springs of length L_0 (in neutral position) placed orthogonally in serial configuration. The geometry is chosen such that both springs are in their neutral positions when points P and O are coincident.

4.1. The 1-DOF parallel spring stage

The basic building block of our design is the linear spring, and this can be refined by replacing linear springs with 1-DOF parallel spring stages, as shown in Fig. 4. The point is that parallel spring
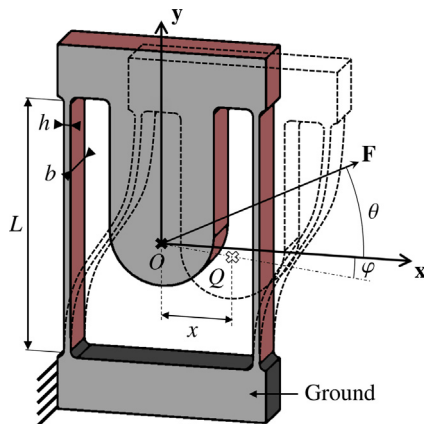

Fig. 4. 1-DOF parallel spring stage.

stages have the advantage of having a simple compact architecture so are easy to manufacture and downscale [16].

As it constitutes the main building block of our central spring designs, we present an extensive analysis of this architecture in order to fully describe its stiffness and kinematic properties.

Fig. 4 consists of two parallel leaf springs (blades) attached to the ground and to a mobile rigid body whose position is uniquely determined by the image of the point $O = (0,0)$. Note that the point O lies exactly half way along the vertical leaf springs, that is, at height $L/2$ from the ground (this satisfies one of the main conditions of Appendix). As defined previously, when a force $\mathbf{F}$ is applied at point $O = (0,0)$ it moves to $Q = (x, y)$, as illustrated in Fig. 4. The force $\mathbf{F}$ can be decomposed into horizontal and vertical components

$$\mathbf{F} = (F_x, F_y) = (F \cos\theta, F \sin\theta),$$

where θ is the angle between the horizontal x-axis and $\mathbf{F}$. We assume that deformations are sufficiently small so that beam shortening theory, as described in [8, Section 8.7], can be applied. As a consequence, and as shown in Appendix A, the effective stiffness $k_x = F_x/x$ along the x-axis is very well approximated by the linearized approximation to the analytic model

$$k_x = \frac{24EI}{L^3} + \frac{6F_y}{5L}, \tag{2}$$

where $I = bh^3/12$, E is the Young modulus of the material and h, b, L are the thickness, the width and the length of the beam, respectively.

Remark 4.1.1. Strictly speaking, formula (2) is an abuse of notation since it refers to an approximation of the horizontal stiffness k_x. In Appendix, we make this difference explicit by referring to k_x as the actual stiffness, k_x^{com} the complete analytic stiffness and k_x^{lin} as the linearized analytic stiffness given in formula (2).

Remark 4.1.2. The necessary condition that the force $\mathbf{F}$ be applied at the mid-height of the beam length $L/2$ will hold for all the mechanism architectures presented in this paper.

Remark 4.1.3. Formula (2) shows that for this structure, the stiffness k_x depends on F_y which means that this spring is sensitive to a force applied along the y-axis. Formula (2) also shows that the influence of F_y on the horizontal stiffness k_x can be reduced by increasing the beam length L.

The other result we will use concerning the 1-DOF parallel spring stage is that, as shown in Appendix A.12, *the trajectory of the rigid block is parabolic* since its defining point $Q = (x, y)$ is very well approximated by

$$\left(x, -\frac{3x^2}{5L}\right). \tag{3}$$

Remark 4.1.4. We note that our formula (2) for the horizontal stiffness is derived using Euler–Bernoulli theory, so as is standard in this theory, the vertical displacement of the mobile block is considered negligible and taken to be zero. *The parabolic trajectory computation included above is used exclusively for the computation of the kinematics.*

4.2. The simple 2-DOF parallel spring stage

In order to get a 2-DOF central spring, two parallel spring stages are therefore placed orthogonally and in a serial configuration, as shown in Fig. 5.

For a radial force $\mathbf{F}$ acting in the x–y plane and applied at angle θ with respect to the x-axis, the displaced position $Q = (x, y)$ of the
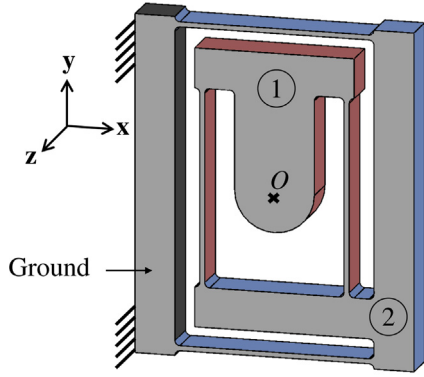
Fig. 5. Simple 2-DOF parallel spring stage.

center of the mechanism is obtained by summing the contribution of the 1-DOF parallel spring stages ① and ②

$$x = x_1 + x_2, \quad y = y_1 + y_2,$$

where, by the results stated in the previous section,

$$x_1 = \frac{F_x}{k_x}, \quad y_1 = \frac{-3x_1^2}{5L}, \quad x_2 = \frac{-3y_2^2}{5L}, \quad y_2 = \frac{F_y}{k_y}.$$

Moreover, as before

$$k_x = \frac{24EI}{L^3} + \frac{6F_y}{5L}, \quad k_y = \frac{24EI}{L^3} + \frac{6F_x}{5L},$$

where once again

$$\mathbf{F} = (F_x, F_y) = (F \cos \theta, F \sin \theta).$$

Combining these results is once again a straightforward computation which yields the following expression for x and y in terms of the force angle θ

$$x = \frac{F \cos \theta}{\frac{2Ebh^3}{L^3} + \frac{6F \sin \theta}{5L}} - \frac{3}{5L} \left(\frac{F \sin \theta}{\frac{2Ebh^3}{L^3} + \frac{6F \cos \theta}{5L}} \right)^2,$$

$$y = \frac{F \sin \theta}{\frac{2Ebh^3}{L^3} + \frac{6F \cos \theta}{5L}} - \frac{3}{5L} \left(\frac{F \cos \theta}{\frac{2Ebh^3}{L^3} + \frac{6F \sin \theta}{5L}} \right)^2.$$

4.3. Compound 2-DOF parallel spring stage

In Section 4.1 we showed that the parallel leaf spring stage has parabolic displacement, however, as pointed out in Section 4.1, isotropic harmonic oscillator solutions are built from orthogonal linear oscillators. We remedy this situation by using the compound parallel spring stage shown in Fig. 6. When force is applied along the **x** direction only, the second order terms of each stage exactly cancel as $F_y = 0$, their stiffness along the x-axis are equal and the second order term y of each stages are of same amplitude, resulting in perfect rectilinear motion.

The same holds in the **y** direction, so the compound 2-DOF parallel stage yields a faithful mechanization of the isotropic harmonic oscillator's x and y components, each taken separately, and is therefore a good candidate for the minimization of isotropy defect. The compound 2-DOF parallel spring stage is illustrated in Fig. 7.

If a constant radial force F is applied at angle θ, then the position of the center O of the compound 2-DOF parallel spring stage is displaced by the action of the four parallel leaf spring stages, these are
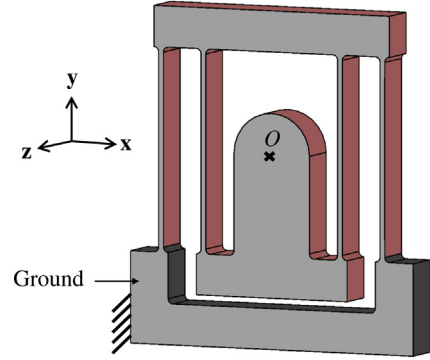
numbered ① to ④ in Fig. 7. The resulting position $Q = (x, y)$ satisfies

$$x = x_1 + x_2 + x_3 + x_4, \quad y = y_1 + y_2 + y_3 + y_4,$$

and writing $\mathbf{F} = (F_x, F_y)$ as before yields

$$x_1 = \frac{F_x}{k_{x1}}, \quad x_2 = \frac{F_x}{k_{x2}}, \quad y_3 = \frac{F_y}{k_{y3}}, \quad y_4 = \frac{F_y}{k_{y4}},$$

$$y_1 = \frac{3x_1^2}{5L}, \quad y_2 = -\frac{3x_2^2}{5L}, \quad x_3 = -\frac{3y_3^2}{5L}, \quad x_4 = \frac{3y_4^2}{5L},$$

where

$$k_{x1} = \frac{24EI}{L^3} - \frac{6F_y}{5L}, \quad k_{x2} = \frac{24EI}{L^3} + \frac{6F_y}{5L},$$

$$k_{y3} = \frac{24EI}{L^3} + \frac{6F_x}{5L}, \quad k_{y4} = \frac{24EI}{L^3} - \frac{6F_x}{5L}.$$

Note that the first expression makes it clear that the four parallel springs can be assembled sequentially in any order. Therefore the compound spring mechanism can be obtained by combining two simple spring mechanisms with the correct orientation.

4.4. Prototype design

In order to evaluate these two central springs, we manufactured two prototypes illustrated in Figs. 8 and 9. The prototypes are composed of aluminum frames and spring steel (X10CrNi18-8) blades whose geometric and material Young modulus are given in Table 1. The aluminum frames of the prototypes were machined with a numerically controlled machining tool and the flexible blades were laser cut. The blade manufacturing and assembly tolerances are
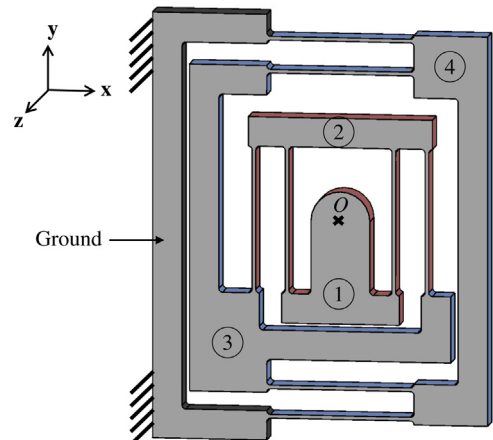

Fig. 6. Compound parallel spring stage.

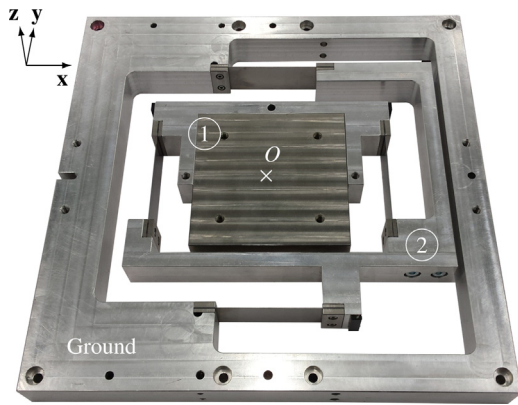**Fig. 7.** In plane orthogonal compound parallel spring stages invention, top view.

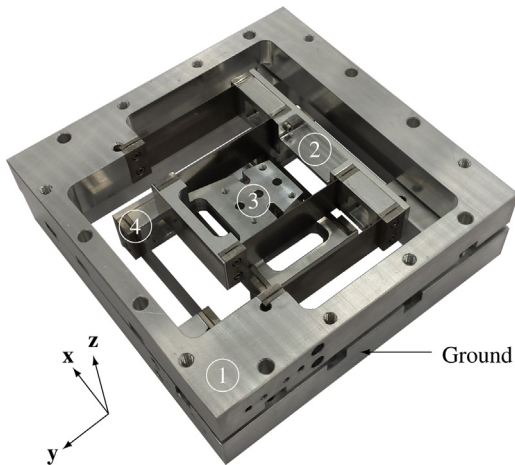**Fig. 8.** Simple 2-DOF parallel spring stage prototype. Frame dimensions $220 \times 220\,mm^2$.

Fig. 9. Two stages assembled for the 2-DOF compound planar spring prototype. Frames dimensions $150 \times 150\,mm^2$.

Table 1
Flexible beam geometric and material parameters for each prototype.

	b [mm]	h [mm]	L [mm]	E [GPa]
Prototype 1	20	0.2	50	200
Prototype 2	20	0.3	50	200

$\pm 7\,\mu m$ and $\pm 60\,\mu m$ for the thickness h and for the length L, respectively. The compound 2-DOF parallel spring stage is composed of two layers, as illustrated in Fig. 10. Each layer gives one DOF in the **x** and **y** directions, respectively. The bottom layer frame is rigidly
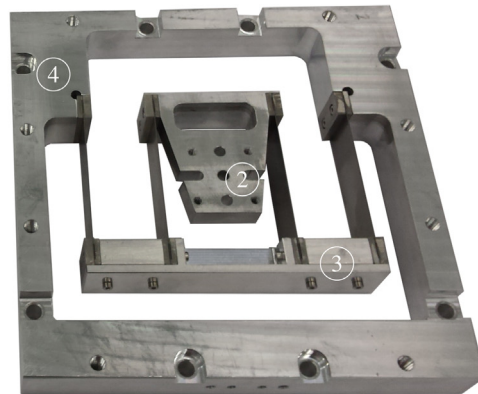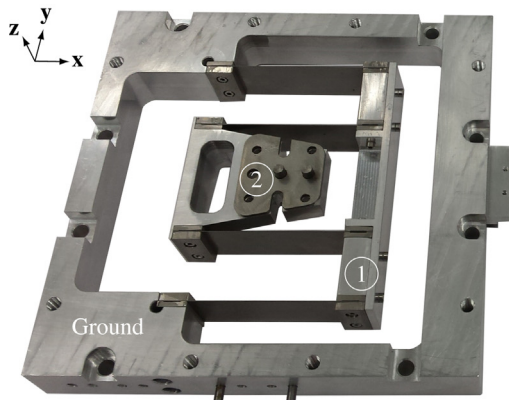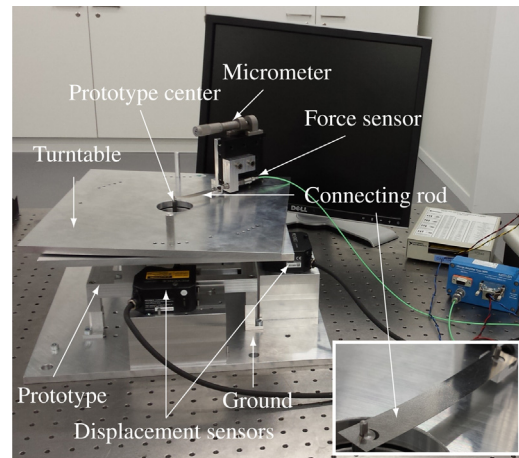

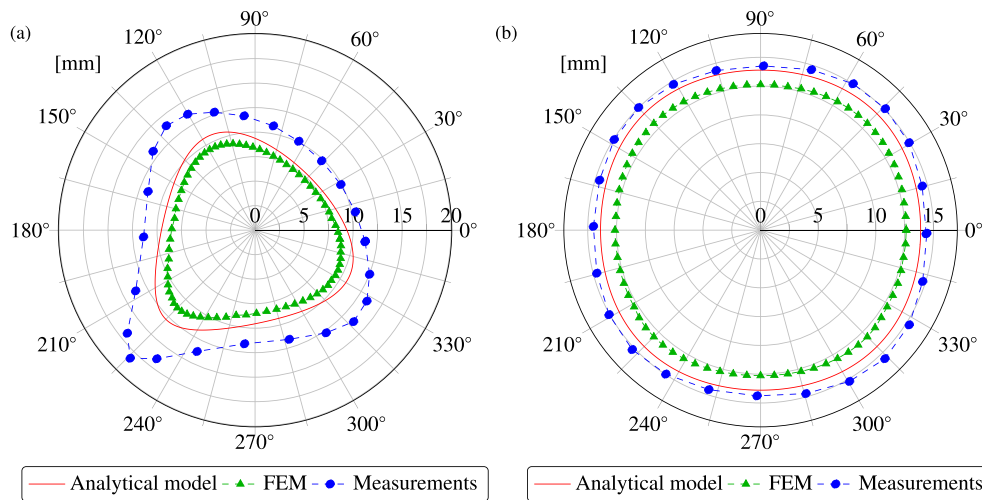**Fig. 11.** Experimental setup with simple 2-DOF spring stage prototype.

fixed to the ground and the top layer frame is the mobile platform marked ④. The layers are connected though the center elements marked ②, see Fig. 10.

5. Experimental evaluation

5.1. Experimental setup

The experimental setup is shown in Fig. 11. The prototype is rigidly fixed to the ground. The center of the moving platform is connected to a force sensor (Kistler 9207) by a flexible beam which acts as a connecting rod. The force sensor is mounted on a linear stage driven manually by a Vernier micrometer (Newport SM-25) which has theoretical displacement resolution of $1\mu m$; its role is to impose a displacement on the prototype center.

This system is fixed on a turntable, that is to say, a table allowing the displacement direction to be varied by $15 \pm 0.04°$. For each orientation, an increasing displacement is applied to the prototype center by actuating the micrometer. The force sensor has an absolute precision of 0.8598 mN with a decreasing drift of 0.5 mN/s. The x and y positions of the moving platform are measured thanks to two displacement sensors: Keyence laser head LK-H082 having measurement range of ± 18 mm and absolute precision of $\pm 7.3\,\mu m$. Data is acquired with an acquisition card (NI PCI-6052E) and associated to the measured force through a Labview software program, where a 3.30 GHz Intel Core i5-2500 computer with 64-bit architecture is used.

Fig. 10. Two layers of the compound 2-DOF parallel spring stage prototype. Frames dimensions $150 \times 150\,mm^2$.

Fig. 12. Polar plots of displacement, in millimeters, of the center of each mechanism. (a) Center displacement, simple 2–DOF spring stage, 5N. (b) Center displacement, compound 2–DOF spring stage, 12N.

5.2. Load case description

Measurements from 1 N to 5 N with 1 N steps were made on the first prototype. Measurements from 1 N to 12 N with 1 N steps were made on the second prototype. Both prototype measurements were made with force directions going from 0° to 345° in 15° steps.

The measurement of stiffness in a single direction takes about 10 s for each force level, which means that for measurements up to 5 N, the force sensor exhibits a drift error of 2.5 mN (0.05% error) and for measurements up to 12 N, the force sensor exhibits a drift error of 6 mN (0.05% error).

6. Results

6.1. Analytical versus numerical and experimental data

Three different type of methods were used to create data describing the mechanism.

6.1.1. Analytical model

The analytical model of Section 4 was implemented using the spring parameters given in Table 1. The resulting data was computed using Matlab. Each plot is given with angular 1° steps.

6.1.2. Finite element model

Finite element analysis (FEA) was done using Comsol, with 1 N force steps, 5° orientation steps and a 0.001 convergence factor. The simple and compound 2-DOF parallel spring stage were computed up to 5 N and 12 N respectively. The simulations were based on non-linear models. Total computation time for the simple and compound 2-DOF parallel spring stage was about 6 days and 9 days, respectively, on a 6 cores (12 threads) Xeon processor cadenced at 3.2 GHz with 48 GB of RAM.

6.1.3. Experimental measurements

The displacement of each prototype's center as a function of force direction was acquired for all force levels. The Vernier micrometer is actuated manually and the data is acquired automatically. Total acquisition time for the simple and compound 2-DOF parallel spring stages was approximately 1.5 and 2 h, respectively.

6.2. Data plots

6.2.1. Displacement polar plots

Displacement polar plots display in polar coordinates the displaced positions Q of the center of each mechanism for a range of force orientations, where Q refers to the notation of Section 3.2.
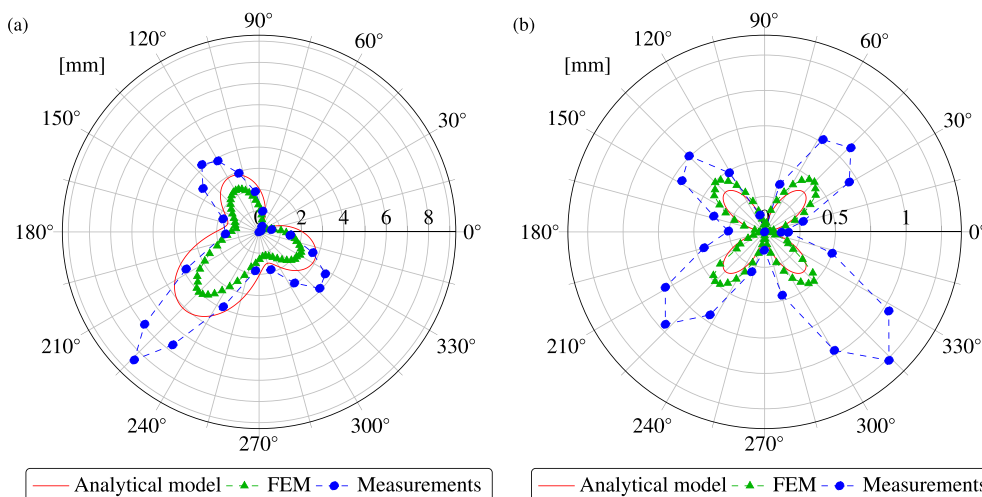
Fig. 13. Polar plots of radial isotropy defect, analytical model, FEM and prototype. (a) Radial isotropy defect in millimeters for the simple 2-DOF parallel spring stage for 5N radial force. (b) Radial isotropy defect in millimeters for the compound 2-DOF parallel spring stage for 12N.
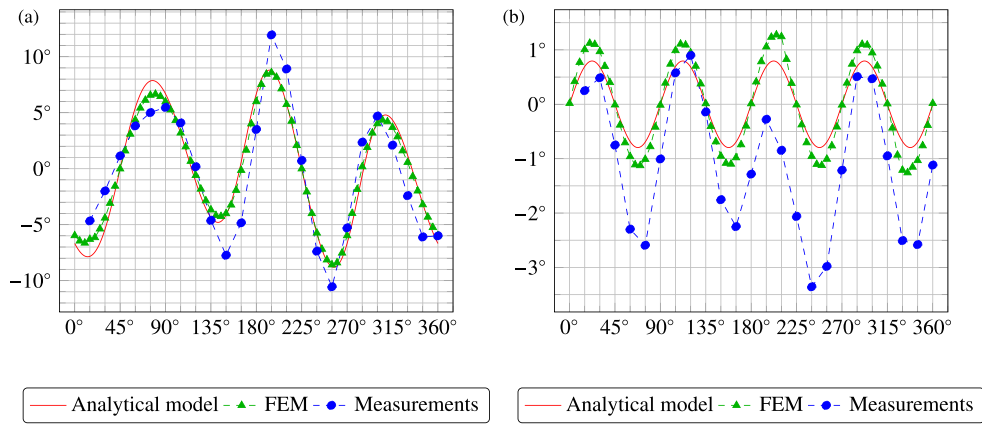
Fig. 14. Angular displacement as a function of force direction, analytical model, FEM and prototype. (a) Simple 2-DOF parallel spring stage under 5N load. (b) Compound 2-DOF parallel spring stage under 12N load.

Fig. 12(a) shows the displaced positions of the center of the simple 2-DOF parallel spring stage as predicted by the analytical model, computed by FEA and measured experimentally with the prototype under a 5 N load. Fig. 12(b) shows the displaced positions of the center of the compound 2-DOF parallel spring stage as predicted by the analytical model, computed by FEA and measured with the prototype under a 12 N load.

Remark 6.2.1. The stiffness properties of the prototypes are very sensitive to the length and thickness tolerances of the blades since these parameters appear to the third power in the stiffness formulation. Thus, manufacturing and assembly tolerances are sufficient to explain discrepancies compared to the model, see Section 4.4.

6.2.2. Radial isotropy defect

Recall from Section 3.2 that the radial isotropy defect was quantified by ρ. In order to plot the radial isotropy, for each given force, a constant independent of θ is subtracted from the measured distances, with the force angle varying from 0° to 360°. This constant value is chosen as the minimum of the measured distances for that given force. This choice appears to give the most readable plot.

The resulting plots for the simple 2-DOF parallel spring stage are illustrated in Fig. 13(a). Here, the maximal radial isotropy defects for the analytical model and the experimental measurements are 65.36% and 86.04%, respectively, of the minimum displacement distance.

The same plot for the compound 2-DOF parallel spring stage, again with the displacement distance offset equal to the minimum displacement distance, is plotted in Fig. 13(b). Here, the maximal

radial isotropy defect for the analytical model and the prototype are to 2.92% and 8.87%, respectively, of the minimum displacement distance.

6.2.3. Angular isotropy defect

Recall from Section 3.2 that the angular isotropy defect was quantified by φ. Fig. 14(a) and (b) plots the angular isotropy defect for each spring. Recall that this quantifies the angular displacement of the center of the mechanism when a radial force is applied.

These plots show that for the simple 2-DOF parallel spring stage, a 0° angular isotropy defect is expected at 45°, 116°, 164°, 225°, 287° and 335° and a maximum angular isotropy defect is expected at 194°.

For the compound 2-DOF parallel spring stage, a 0° angular isotropy defect is expected at 0°, 45°, 90°, 135°, 180°, 225°, 270° and 315°, and a maximum isotropy defect is expected at the midpoint of these angles, that is, at 22.5°, 22.5°+45°, 22.5°+90°,..., 22.5°+315°.

6.2.4. Stiffness isotropy

Recall the definition of k_θ in Section 3.2 which shows that the isotropy defect Δk can represented by plotting stiffness k_θ as a function of force direction θ. For a perfectly isotropic spring, this should be constant and the plot a horizontal line. Fig. 15(a) and (b) illustrates stiffness as a function of force direction for the simple and compound 2-DOF parallel spring stages.
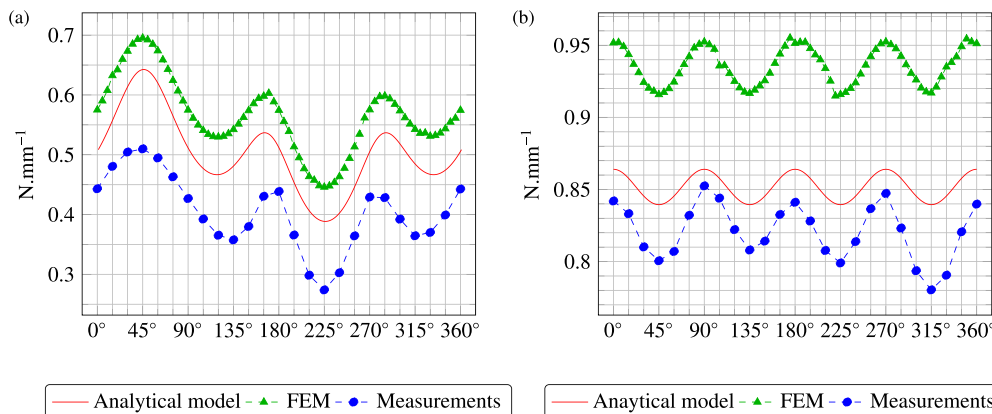
Fig. 15. Stiffness as a function of force direction for each mechanism. (a) Simple 2-DOF parallel spring stage up to 5N load. (b) Compound 2-DOF parallel spring stage up to 12N load.
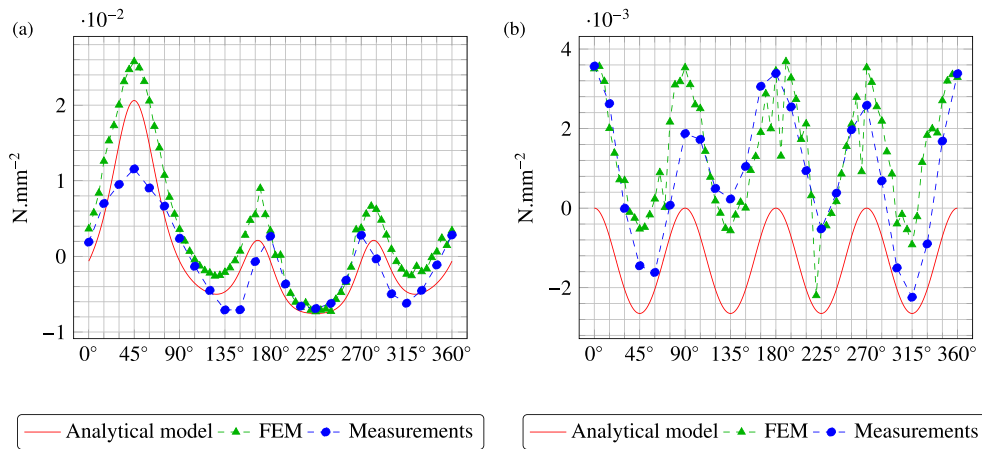
Fig. 16. Second order term of stiffness polynomial fit as a function of force direction. (a) Simple 2-DOF parallel spring stage up to 5N load. (b) Compound 2-DOF parallel spring stage up to 12N load.

6.2.5. Stiffness linearity

We recall the stiffness linearity assumptions and notation of Section 3.2. We focus here on the second order term C_θ quantifying the stiffness linearity defect. In Fig. 16, a polynomial fit for C_θ is given for each central spring. Fig. 16(a) shows that the simple 2-DOF parallel spring stage has a non-linearity defect ten times greater than the compound 2-DOF parallel spring stage shown in Fig. 16(b). Moreover, the simple 2-DOF parallel spring stage has both positive and negative second order terms whereas the compound 2-DOF parallel spring stage has only negative order terms.

The simple 2-DOF parallel spring stage is also highly non-linear in the 45° and 225° directions. Therefore, the simple 2-DOF parallel spring stage has both non-linearity and stiffness isotropy defects.

## 7. Improved mechanism architectures

With the goal of reducing isotropy defect, one can improve the performance of the simple and compound mechanisms by placing an additional copy in parallel, at the cost of a loss of simplicity and planarity. The following results were obtained from the analytical model.

For the simple mechanism, one places in parallel a second identical copy which is rotated 180° in-plane (Fig. 18(a)). This is done in order to cancel out the minimal and maximal stiffness values found in Fig. 15(a) and leads to an isotropy defect η_{max} of 6.77% instead of 65.36%, with η_{max} as defined in Section 3.2. In order to compare stiffness isotropy defects of the original versus the double mechanism, the compound mechanism has its leaf spring beams stiffness divided by two (e.g., beam width halved) and the comparison is shown in Fig. 17(a). For the same reason, when the serial arrangement is considered, the leaf spring beams stiffness is multiplied by two (e.g., beam width doubled).

An even greater improvement is possible for the compound mechanism by placing a parallel copy at 45° (Fig. 18(b)). This cancels out the minimal and maximal stiffness values shown in Fig. 15(b) and yields an isotropy defect η_{max} of only 0.0262% instead of 2.92%. This pair of compound mechanism is 111 times more isotropic than the single structure. Once again, a comparison of stiffness for the single versus the compound mechanism is possible by halving the leaf spring stiffness of the compound mechanism with the results shown in Fig. 17(b).

This process can be continued by further combining 22.5° parallel in-plane rotations of four compound mechanisms to cancel out minimal and maximal stiffness. The isotropy defect could thus be reduced to $\eta_{max} = 1.58\,e^{-6}$% by stacking together four layers of compound mechanisms with the above orientation. Stacking four compound mechanisms is 16,567 times better than stacking two compound mechanisms and 1,847,200 times better than
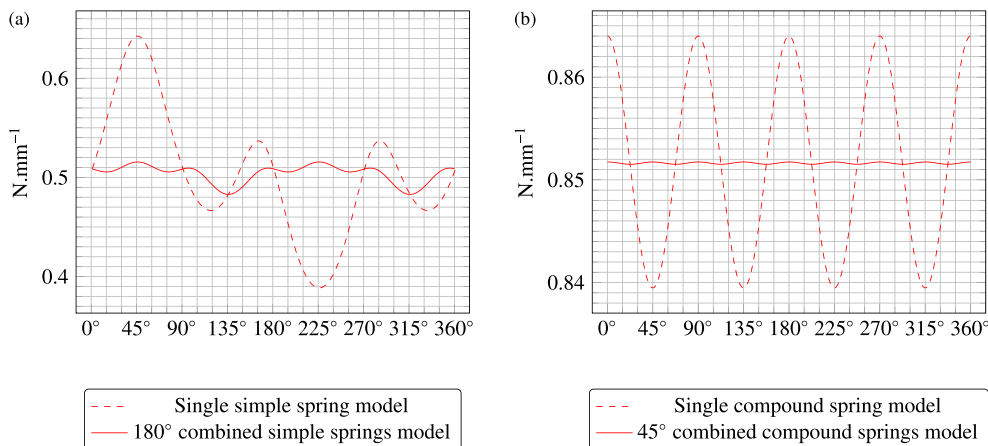
Fig. 17. Stiffness of parallel central springs with isotropy defect reduction. (a) Stiffness of 180° parallel simple 2-DOF parallel spring stages as a function of direction. (b) Stiffness of 45° parallel compound 2-DOF parallel spring stages as a function of direction.
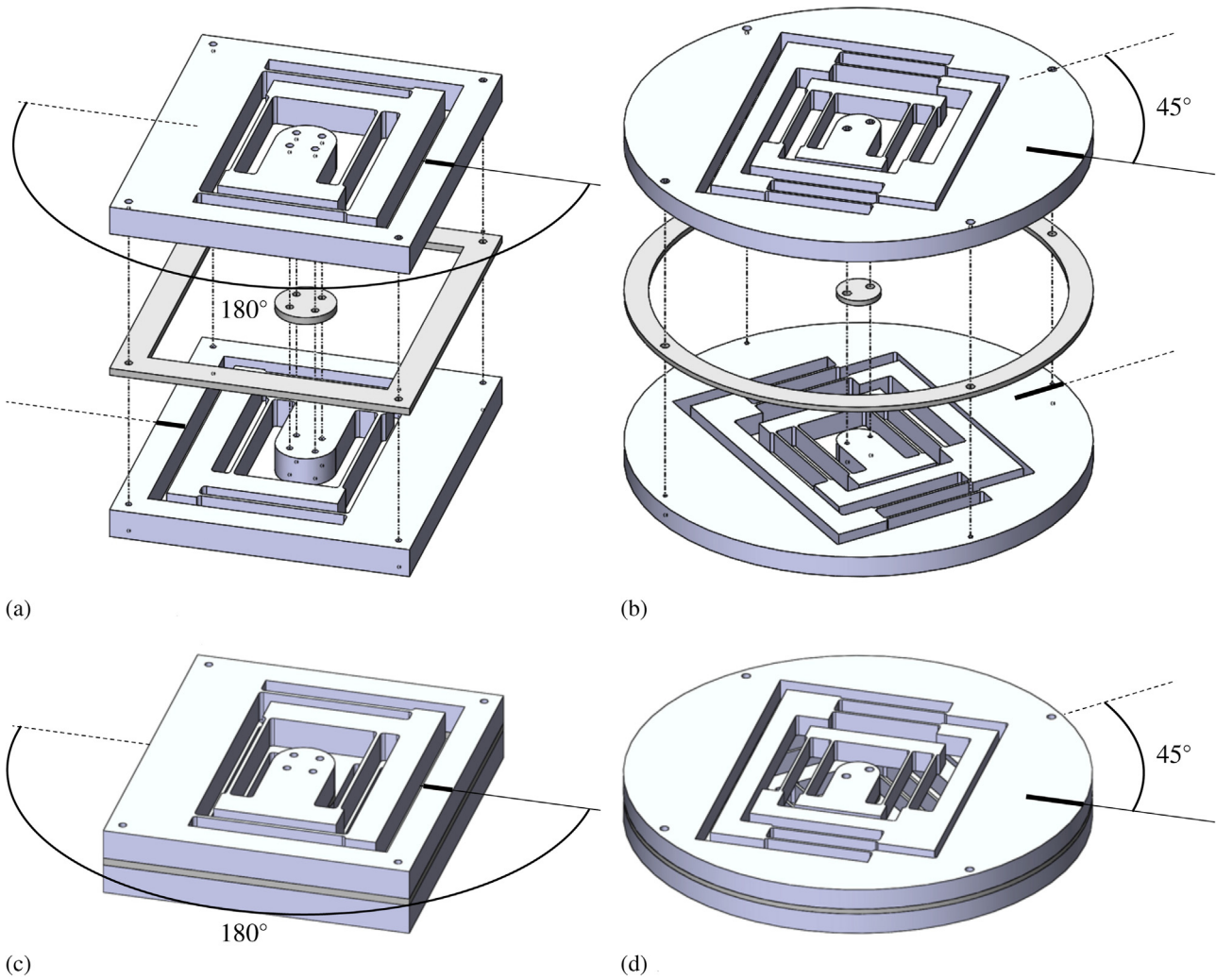
Fig. 18. Possible realizations of parallel central spring arrangement decreasing isotropy defect. (a) Exploded view of realization of the 180° parallel arrangement of simple 2-DOF parallel spring stages, top view. (b) Exploded view of realization of the 45° parallel arrangement of compound 2-DOF parallel spring stages, top view. (c) Realization of the 180° parallel arrangement of simple 2-DOF parallel spring stages, top view. (d) Realization of the 45° parallel arrangement of compound 2-DOF parallel spring stages, top view.

Table 2
Stiffness isotropy defect η_{max} comparison between the single and multi-layer parallel arrangement of the simple and compound 2-DOF spring stages.

# of stages	Simple				Compound			
	η_{max}	Defect reduction factor	# global max	Stage offset	η_{max}	Defect reduction factor	# global max	Stage offset
1	65.36%	1	1	–	**2.92%**	1	4	–
2	6.77%	9.66	2	180°	$2.62e-2$%	111.53	8	45°
4	**1.87%**	35.02	4	90°	$1.58e-6$%	$1.85e6$	16	22.5°
8	0.11%	578.26	8	45°	$1.04e-13$%	$28e12$	32	11.25°

Table 3
Stiffness isotropy defect η_{max} comparison between the single and multi-layer serial arrangement of the simple and compound 2-DOF spring stages.

# of stages	Simple				Compound			
	η_{max}	Defect reduction factor	# global max	Stage offset	η_{max}	Defect reduction factor	# global max	Stage offset
1	65.36%	1	1	–	2.92%	1	4	–
2	5.41%	12.08	4	180°	$5.46e-3$%	535.60	8	45°
4	5.16%	12.66	4	90°	$3.81e-7$%	$1.40e9$	16	22.5°
8	$4.99e-2$%	1310.41	8	45°	$5.21e-14$%	$56.01e12$	32	11.25°
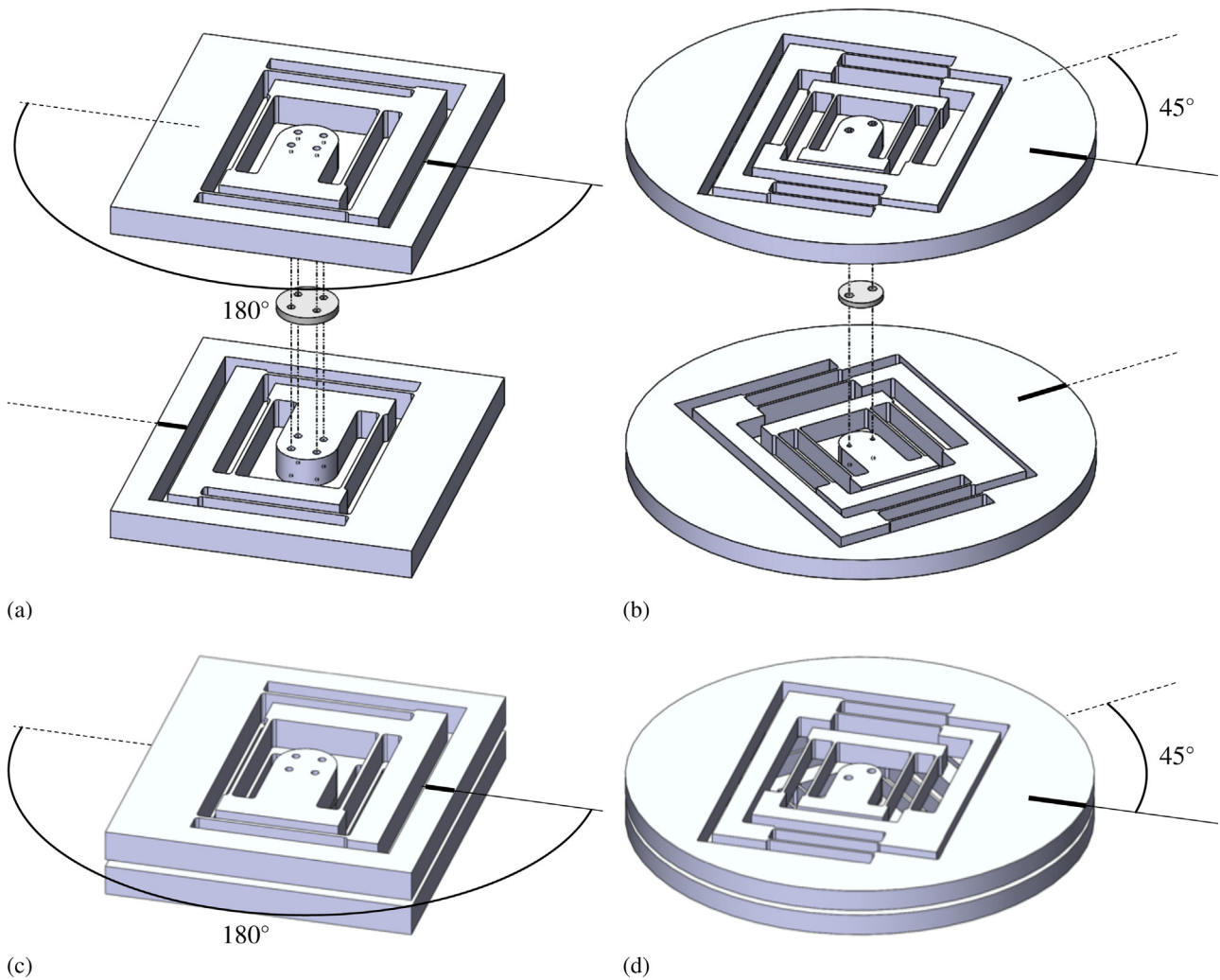
Fig. 19. Possible realizations of serial central spring arrangement decreasing isotropy defect. (a) Exploded view of realization of the 180° parallel arrangement of simple 2-DOF parallel spring stages, top view. (b) Exploded view of realization of the 45° parallel arrangement of compound 2-DOF parallel spring stages, top view. (c) Realization of the 180° parallel arrangement of simple 2-DOF parallel spring stages, top view. (d) Realization of the 45° parallel arrangement of compound 2-DOF parallel spring stages, top view.

the single compound mechanism. For both architectures, the performances of parallel rotated arrangement are presented in Table 2.

A possible realization for each central springs combining two layers, 180° and 45° rotation respectively, is illustrated in Fig. 19. In order to avoid contact between the intermediate parts, shims are placed between the two layers connected rigidly to the frames (ground) and moving platforms ① (see Figs. 5 and 7). Note that the roles of the moving platform and of the ground can be inverted.

Further iterations reduce the isotropy defect to arbitrarily small values.

Remark 7. Another method for reducing the isotropy defect is to stack two stages in series at specific shift angles. The resulting improvement is quantified in Table 3.

8. Conclusion

The number, position and value of local maximums as predicted by the analytical model and the FEM model are consistent and they match the experimental results. This validates the use of the simple analytical model established in Section 4 to predict the isotropy performance of such structures.

Tables 2 and 3 show that the isotropy defect of the original simple spring stage can be drastically reduced using two approaches

- Use of compound stages instead of simple stages.
- Parallel or serial stacking of identical stages rotated by precisely chosen angles.

For the parallel arrangements, the quantitative evaluation of these designs shows that stacking four simple stages leads to a maximum relative stiffness isotropy defect close to that of a single compound stage (values shown in boldface in the table).

For example, Fig. 18 shows how pairs of simple and compound stage having maximum relative stiffness isotropy defects 65.36% and 2.92%, respectively, can be stacked leading to a decrease of the relative stiffness isotropy defect by a factor 9.66 and 111.53, respectively, leading to relative residual defects of 6.77% and 0.0262%.

Appendix A. Stiffness and kinematics of the 1-DOF parallel spring stage

In this Appendix, we give a formal, self-contained proof of the claims of Section 4.1. In other words, we will show that given the 1-DOF parallel spring stage shown in Fig. A.20, horizontal stiffness k_x is very well approximated by

$$k_x^{\text{lin}} = \frac{24EI}{L^3} + \frac{6F_y}{5L},$$

and that the rigid block has a parabolic trajectory since the coordinates of the distinguished point $Q = (x, y)$ is very well approximated by

$$\left(x, -\frac{3x^2}{5L} \right).$$

Note that, as stated in Remark 4.1.4, our formula for the horizontal stiffness is derived using Euler–Bernoulli theory, so the vertical displacement of the mobile block is considered negligible. The parabolic trajectory computation included above is used exclusively for the computation of the kinematics.

A.1. Plan of proof

The proof applies standard methods of mechanics of materials, e.g., as found in [8].

We examine the situation illustrated in Fig. A.20, in which a horizontal force is applied to a parallel spring stage when a vertical load is present. Clearly this vertical load affects the horizontal stiffness, and making this explicit will be the focus of our investigation.

The general idea of the proof is to consider a single beam, use Euler–Bernoulli theory to compute the horizontal deformation at the beam extremity for a given horizontal force and vertical load, recover the horizontal stiffness using Hooke's Law, then multiply by two to get the total horizontal stiffness.

The vertical tension and compression cases lead to completely different analytic solutions, despite giving the same result for the linearized horizontal stiffness, so we will take care to distinguish these cases in this Appendix.

Our computations up to and including Appendix A.9 are complete analytic expressions with linearization only occurring in Appendix A.10 to Appendix A.12.

We begin the proof in Appendix A.2 with an explicit description of the parameters involved and note that three vertical load situations occur.

In Appendix A.4, we begin the computation by considering only a single beam of our model. We then set up the known governing differential equations of deformation for each of the three load situations.

In Appendix A.5, we give the known general analytic solutions to the differential equations of Appendix A.4.
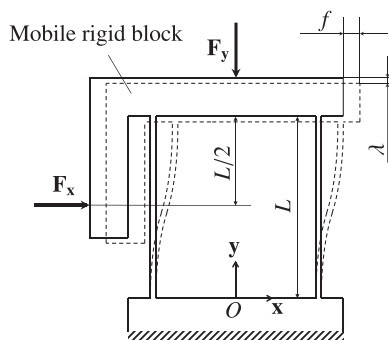

Fig. A.20. Parallel spring stage under load.

In Appendix A.6, we apply the boundary conditions in order to compute the complete analytic solutions to our three load situations.

In Appendix A.7, we compute, for our three load situations, the horizontal restoring force for a given horizontal displacement of a single beam extremity (which is exactly the displacement of the mobile rigid block).

In Appendix A.8, we apply Hooke's law to the result of Appendix A.7 to derive the complete analytic expression for the horizontal stiffness of a single beam at its extremity, and this for our three load situations.

In Appendix A.9, we apply the result of Appendix A.8 to find an complete analytic solution to the horizontal stiffness for the 1-DOF parallel spring stage given our three vertical load situations. This gives the complete analytic solution to our main problem.

In Appendix A.10, we give the linearization of the formulas of Appendix A.9 completing the proof of the first main result of this Appendix.

In Appendix A.11, we give a numerical estimate of the relative error between the complete analytic expression and its linearization used in the paper and show that it is bounded by 404ppm.

Appendix A.12 is independent of the previous analysis and is based on well-known results of beam deformation theory. These known results yield the vertical and horizontal displacements of the beam extremities in our model, and approximating to second order yields the parabolic trajectory, the second main result of this Appendix.

A.2. Problem description

The two vertical beams in Fig. A.20 are identical and have a moment of inertia I around $\mathbf{z}$, and Young's modulus E. The horizontal displacement of the mobile rigid block is given by F and its vertical displacement by λ. Note that, by Hooke's Law, the horizontal stiffness of the model is simply $k_x = F_x/f$, where $\mathbf{F}_x = F_x\mathbf{x}$.

Our goal is to find a simple approximation to the horizontal stiffness k_x. Our approach will be to apply Euler–Bernoulli theory to find a complete analytic formula k_x^{com} for this horizontal stiffness and use its linearized value k_x^{lin} as our simple approximation. We will keep the superscripts explicit during our entire computation in order to minimize confusion regarding the three different values of horizontal stiffness: exact, complete Euler–Bernoulli and linearized Euler–Bernoulli.

Since the technical evaluation of total horizontal stiffness is carried out for a single beam, we denote the horizontal stiffness of a single beam by κ_x, its complete analytic formula κ_x^{com} and its linearized value κ_x^{lin}.

In the technical discussion that follows, it is necessary to distinguish three vertical (axial) load situations. Writing $\mathbf{F}_y = F_y\mathbf{y}$, we have

1. No vertical load: $F_y = 0$.
2. Vertical tensile load: $F_y > 0$.
3. Vertical compression load: $F_y < 0$.

In order to distinguish these cases in the computations below, it will be convenient to work with the magnitude $F_y^{\text{abs}} = |F_y|$ of F_y.

A.3. Reduction to single beam

The technical part of the proof will be established by considering a single beam on the structure of Fig. A.20. This reduction is possible since the horizontal stiffnesses of the two beams are identical and the total horizontal stiffness of the structure is exactly twice the horizontal stiffness of each beam.

To show that this is true, first note that the horizontal force is applied to the rigid block at vertical height $L/2$, and that the torque at $L/2$ vanishes. This means that no spurious vertical force is

generated and that no torque is applied to the mobile rigid block. It follows that the block does not exhibit parasitic rotations and moves translationally only.

It follows from the previous paragraph that the vertical load on each beam is identical. Since the two beams are geometrically identical, their stiffnesses are also identical in the special case of horizontal force applied at height $L/2$. This justifies our study of a single beam.

Since the mechanism has a parallel architecture, the magnitude of the load carried by one beam becomes $F_y^{abs}/2$.

It then follows that the total horizontal stiffness of the 1-DOF parallel spring stage under a vertical load is recovered by multiplying the single beam horizontal stiffness by two, as claimed at the beginning of this section.

A.4. Setting up the differential equation

The governing differential equation of the deformation of an Euler–Bernoulli beam under load and up to the fourth derivative is well-known [8, p. 464, p. 591]

$$EIx^{(4)} - \frac{F_y}{2}x'' = 0.$$

For our three load situations, this gives
1. No vertical load:

$$EIx^{(4)} = 0.$$

2. Vertical tensile load:

$$EIx^{(4)} - \frac{F_y^{abs}}{2}x'' = 0.$$

3. Vertical compression load:

$$EIx^{(4)} + \frac{F_y^{abs}}{2}x'' = 0.$$

A.5. General beam deflection solution

The beam deflection solutions for the three vertical load situations are as follows, where $\omega = \sqrt{F_y^{abs}/(2EI)}$.
1. No vertical load:

$$x_0 = a_0 + a_1 y + a_2 y^2 + a_3 y^3. \tag{A.1}$$

2. Vertical tensile load:

$$x_t = b_0 + b_1 y + b_2 \cosh(\omega y) + b_3 \sinh(\omega y).$$

3. Vertical compression load:

$$x_c = c_0 + c_1 y + c_2 \cos(\omega y) + c_3 \sin(\omega y).$$

A.6. Boundary conditions

The beam extremities of our model satisfy the following boundary conditions.

$$x(0) = 0, \quad x'(0) = 0, \quad x(L) = f, \quad x'(L) = 0,$$

where the last boundary condition follows from the fact that the mobile mass does not rotate, as shown in Appendix A.3.

Applying these boundary conditions allows us to compute the constants in the general solutions found in the previous section.
1. No vertical load:

$$a_0 = a_1 = 0, \quad a_2 = \frac{3f}{L^2}, \quad a_3 = -\frac{2f}{L^3}. \tag{A.2}$$

2. Vertical tensile load:

$$b_0 = -\frac{f(\cosh(L\omega) - 1)}{B}, \quad b_1 = \frac{f\omega \sinh(L\omega)}{B},$$
$$b_2 = \frac{f(\cosh(L\omega) - 1)}{B}, \quad b_3 = -\frac{f\sinh(L\omega)}{B},$$

where $B = 2(1 - \cosh(L\omega)) + L\omega \sinh(L\omega)$.
3. Vertical compression load:

$$c_0 = -\frac{f(\cos(L\omega) - 1)}{C}, \quad c_1 = -\frac{f\omega \sin(L\omega)}{C},$$
$$c_2 = \frac{f(\cos(L\omega) - 1)}{C}, \quad c_3 = \frac{f\sin(L\omega)}{C},$$

where $C = 2(1 - \cos(L\omega)) - L\omega \sin(L\omega)$.

A.7. Horizontal force for given horizontal displacement

The differential equation governing the horizontal force at vertical height y is

$$F_x(y) = -EIx^{(3)}(y) + \frac{F_y}{2}x'(y).$$

We are interested in the horizontal force $F_x = F_x(L)$ at the extremity $y = L$ of the beam since it is essentially the restoring force applied to the mobile rigid block. Since $x'(L) = 0$ this reduces to

$$F_x = -EIx^{(3)}(L).$$

The explicit analytic formula found in the previous sections can be applied to find the horizontal force F_x at vertical height $y = L$ which produces the horizontal displacement f, and this for the three vertical load situations.
1. No vertical load:

$$F_x = \frac{12EI}{L^3}f.$$

2. Vertical tensile load:

$$F_x = \frac{EI\omega^3 \sinh(\omega L)}{B}f.$$

3. Vertical compression load:

$$F_x = \frac{EI\omega^3 \sin(\omega L)}{C}f.$$

A.8. Complete horizontal stiffness of a single beam

The complete Euler–Bernoulli horizontal stiffness κ_x^{com} of a single beam is now computed by simply applying Hooke's Law

$$\kappa_x^{com} = \frac{F_x}{f},$$

to the formulas of the previous section for each of the three load cases and performing some elementary trigonometric simplification.
1. No vertical load:

$$\kappa_x^{com} = \frac{12EI}{L^3}. \tag{A.3}$$

2. Vertical tensile load:

$$\kappa_x^{com} = \frac{F_y^{abs}/2}{L - \frac{2}{\omega} \tanh\left(\frac{L\omega}{2}\right)}. \tag{A.4}$$

3. Vertical compression load:

$$\kappa_x^{com} = \frac{F_y^{abs}/2}{\frac{2}{\omega} \tan\left(\frac{L\omega}{2}\right) - L}. \tag{A.5}$$

We see from formula (A.5) that there exists a vertical load v_0 producing zero stiffness exactly when $\omega L = \pi$ so that $v_0 = \frac{\pi^2 EI}{L^2}$.

We then define $\gamma = F_y^{abs}/(2v_0)$ so that $\omega = \frac{\pi}{L}\sqrt{\gamma}$. This allows us to rewrite the stiffness as a multiple of κ_0, the stiffness of one beam without axial load. Note that the superscript κ_0^{com} has been suppressed, since all values of k_0 will be identical in what follows.

1. No vertical load:

$$\kappa_x^{com} = \kappa_0. \tag{A.6}$$

2. Vertical tensile load:

$$\kappa_x^{com} = \kappa_0 \frac{\gamma\pi^2}{12\left(1 - \frac{2}{\pi\sqrt{\gamma}}\tanh\left(\frac{\pi\sqrt{\gamma}}{2}\right)\right)}.$$

3. Vertical compression load:

$$\kappa_x^{com} = \kappa_0 \frac{\gamma\pi^2}{12\left(\frac{2}{\pi\sqrt{\gamma}}\tan\left(\frac{\pi\sqrt{\gamma}}{2}\right) - 1\right)}.$$

A.9. Complete horizontal stiffness of the 1-DOF parallel spring stage

As shown in Appendix A.3, the parallel flexure stage is composed of two identical beams therefore its complete analytical horizontal stiffness is simply $k_x^{com} = 2\kappa_x^{com}$.

It follows that the vertical compression load inducing zero horizontal stiffness is simply $N_0 = 2v_0$ so that

$$N_0 = \frac{2\pi^2 EI}{L^2}.$$

Expressing γ in terms of N_0 gives $\gamma = F_y^{abs}/(2v_0) = F_y^{abs}/N_0$. The total horizontal stiffness for the three load cases, expressed as a function of the no vertical load case k_0, are found by simply multiplying the expressions of the previous section by two.

1. No vertical load:

$$k_x^{com} = k_0 = \frac{24EI}{L^3}.$$

2. Vertical tensile load:

$$k_x^{com} = k_0 \frac{\gamma\pi^2}{12\left(1 - \frac{2}{\pi\sqrt{\gamma}}\tanh\left(\frac{\pi\sqrt{\gamma}}{2}\right)\right)}. \tag{A.7}$$

3. Vertical compression load:

$$k_x^{com} = k_0 \frac{\gamma\pi^2}{12\left(\frac{2}{\pi\sqrt{\gamma}}\tan\left(\frac{\pi\sqrt{\gamma}}{2}\right) - 1\right)}. \tag{A.8}$$

A.10. Linearized horizontal stiffness of the 1-DOF parallel spring stage

In this section, we use the Taylor series expansion of the solutions found in the previous section to linearize the complete analytic stiffness k_x^{com} of the 1-DOF parallel spring stage.

1. No vertical load:

$$k_x^{lin} = k_0 = \frac{24EI}{L^3}.$$

2. Vertical tensile load:
The Taylor expansion of $\tanh(X)$ up to third order gives

$$\tanh\left(\frac{\pi\sqrt{\gamma}}{2}\right) = \frac{\pi\sqrt{\gamma}}{2} - \frac{\pi^3\gamma\sqrt{\gamma}}{24} + \frac{\pi^5\gamma^2\sqrt{\gamma}}{240}$$

so that

$$k_x^{lin} = \frac{k_0}{1 - \frac{\gamma\pi^2}{10}}.$$

Applying the Taylor expansion of $\frac{1}{1+X}$ up to second order gives

$$k_x^{lin} = k_0\left(1 + \frac{\gamma\pi^2}{10}\right) = k_0 + \frac{6}{5L}F_y^{abs}. \tag{A.9}$$

3. Vertical compression load:
The Taylor expansion of $\tan(X)$ up to third order gives:

$$\tan\left(\frac{\pi\sqrt{\gamma}}{2}\right) = \frac{\pi\sqrt{\gamma}}{2} + \frac{\pi^3\gamma\sqrt{\gamma}}{24} + \frac{\pi^5\gamma^2\sqrt{\gamma}}{240}$$

so that

$$k_x^{lin} = \frac{k_0}{1 + \frac{\gamma\pi^2}{10}}.$$

Applying the Taylor expansion for $\frac{1}{1+X}$ up to second order gives

$$k_x^{lin} = k_0\left(1 - \frac{\gamma\pi^2}{10}\right) = k_0 - \frac{6}{5L}F_y^{abs}. \tag{A.10}$$

Finally, one notes that in Eq. (A.9) one has $F_y = F_y^{abs}$ and that in Eq. (A.10) one has $F_y = -F_y^{abs}$, so applying this and substituting the explicit formula for k_0 found in case 1 gives the main result of this Appendix

$$k_x^{lin} = \frac{24EI}{L^3} + \frac{6F_y}{5L},$$

as promised.

A.11. Error estimate

In this section we investigate the discrepancy between the complete analytical stiffness k_x^{com} and the linearized analytical stiffness k_x^{lin} as a function of $\gamma = F_y^{abs}/N_0$.

Let us define $Z^{com}(\gamma) = k_x^{com}/k_0$. Note that $Z^{com}(\gamma)$ expresses the relative discrepancy from the nominal stiffness k_0. We have

1. No vertical load:

$$Z^{com}(0) = 1.$$

2. Vertical tensile load:

$$Z^{com}(\gamma) = \frac{\gamma\pi^2}{12\left(1 - \frac{2}{\pi\sqrt{\gamma}}\tanh\left(\frac{\pi\sqrt{\gamma}}{2}\right)\right)}.$$

3. Vertical compression load:

$$Z^{com}(\gamma) = \frac{\gamma\pi^2}{12\left(\frac{2}{\pi\sqrt{\gamma}}\tan\left(\frac{\pi\sqrt{\gamma}}{2}\right) - 1\right)}.$$

We similarly define $Z^{lin}(\gamma) = k_x^{lin}/k_0$, which again expresses the relative discrepancy from the nominal stiffness k_0.

1. No vertical load:

$$Z^{lin}(0) = 1.$$

2. Vertical tensile load:

$$Z^{lin}(\gamma) = 1 + \frac{\gamma\pi^2}{10}.$$

3. Vertical compression load:

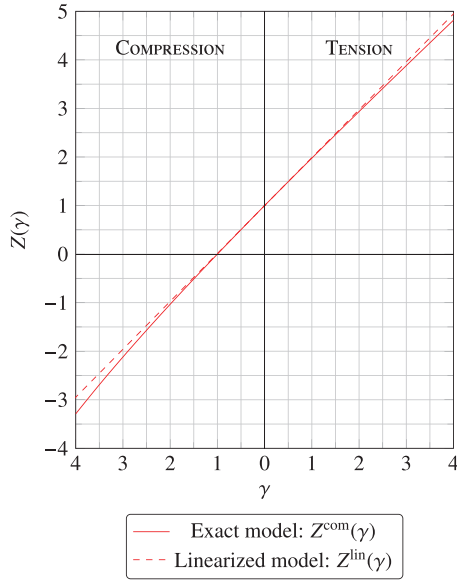$$Z^{lin}(\gamma) = 1 - \frac{\gamma\pi^2}{10}.$$

Fig. A.21. Normalized models comparison.

In Fig. A.21 the two normalized stiffness models $Z^{\text{com}}(\gamma)$ and $Z^{\text{lin}}(\gamma)$ are plotted on the same graph. Note that, by definition, $\gamma \geq 0$.

We define the relative error ε_γ between the complete and linearized model to be

$$\varepsilon_\gamma = \frac{Z^{\text{lin}}(\gamma) - Z^{\text{com}}(\gamma)}{Z^{\text{lin}}(\gamma)} = \frac{k_x^{\text{lin}} - k_x^{\text{com}}}{k_x^{\text{lin}}},$$

so that the relative error ε_γ expresses the relative error in $Z(\gamma)$ as well as in k_x.

For the first prototype's beam dimensions (see Table 1), the load which produces a zero stiffness of the parallel spring stage is $N_0 = 21.05$N. The maximal applied vertical load we consider for this mechanism is $F_y^{\text{abs}} = 5$N, corresponding to $\gamma = 0.2375$, which gives a maximal relative error $\varepsilon_\gamma = 877$ppm.

For the second prototype's beam dimensions, see Table 1, the load which produces a zero stiffness of the parallel spring stage is $N_0 = 71.06$N. The maximal applied vertical load we consider for this mechanism is $F_y^{\text{abs}} = 12$N, corresponding to $\gamma = 0.1689$, which gives a maximal relative error $\varepsilon_\gamma = 404$ppm.

Conclusion. The 1-DOF parallel spring stage linearized analytical horizontal stiffness model used in this paper is a very good approximation to the complete analytical model.

A.12. Parabolic trajectory with no vertical load

As shown in Appendix A.3, the mobile rigid block moves translationally so its position is uniquely described by the position $Q = (x, y)$ of the translated point $O = (0, 0)$. We now show that the trajectory is well approximated by a parabola. In order to do this, we compute the vertical displacement λ of the beam extremity, see Fig. A.20, that is, the difference between the original beam length L before deformation and the length of the deformed beam's projection on the y-axis. As is found in the literature [8, p. 465], λ can be evaluated by the classical formula

$$\lambda \simeq \frac{1}{2} \int_0^L \left(x'(y) \right)^2 dy. \tag{A.11}$$

This formula is established using a truncated power series development, so is valid only for small beam deflection angles.

Taking the derivative of formula (A.1) with respect to y and using the constant values of formula (A.2) we get

$$x'(y) = \frac{6f}{L^2} \left(y - \frac{y^2}{L} \right), \tag{A.12}$$

Using (A.11) and (A.12), we obtain the vertical displacement λ as a function of horizontal translation f

$$\lambda \simeq \frac{3f^2}{5L},$$

which is the equation of a parabola.

References

[1] Awtar S. Synthesis and analysis of parallel kinematic XY flexure mechanisms. Cambridge: Massachusetts Institute of Technology; 2006 [Ph.D. thesis].
[2] Bertrand J. Théorème relatif au mouvement d'un point attiré vers un centre fixe. C R Acad Sci 1873;77:849–53.
[3] Dinesh M, Ananthasuresh GK. Micro-mechanical stages with enhanced range. Int J Adv Eng Sci Appl Math 2010;2:35–43.
[4] Josic K, Hall RW. Planetary motion and the duality of force laws. SIAM Rev 2000;42:114–25.
[5] Henein S, Kjelberg I, Zelenika S. Flexible bearings for high-precision mechanisms in accelerator facilities. In: 26th advanced ICFA beam dynamics workshop on nanometre-size colliding beams. 2002.
[6] Henein S. Conception des structures articulées á guidages flexibles de haute précision. Ecole polytechnique federale de Lausanne; 2000, http://dx.doi.org/10.5075/epfl-thesis-2194 [Ph.D. thesis].
[7] Henein S, Vardi I, Rubbert L, Bitterli R, Ferrier N, Fifanski S, et al. IsoSpring: vers la montre sans échappement. In: actes de la Journée d'Étude de la SSC 2014. 2014. p. 49–58.
[8] Gere JM, Timoshenko SP. Mechanics of materials. 3rd ed. Boston: PWS-KENT; 1990.
[9] Howell LL. Compliant mechanisms. Wiley; 2001.
[10] Huygens C., Horologium oscillatorium [Latin with English translation by Ian Bruce], www.17centurymaths.com/contents/huygenscontents.html
[11] Yangmin Li, Qingsong Xu. Design of a new decoupled XY flexure parallel kinematic manipulator with actuator isolation. IEEE; 2008.
[12] Yangmin Li, Jiming Huang, Hui Tang. A compliant parallel XY micromotion stage with complete kinematic decoupling. IEEE; 2012.
[13] Newton I. The mathematical principles of natural philosophy. Google eBook; 1729 [Andrew Motte, Trans.].
[14] Niaudet N, Breguet LC. Application du diapason à l'horlogerie. Comptes Rendus de l'Académie de Sciences 1866;63:991–2.
[15] Santos FC, Soares V, Tort AC. An English translation of Bertrand's theorem. Lat Am J Phys Educ 2011;5:694–5.
[16] Trease BP, Moon Y-M, Kota S. Design of large-displacement compliant joints. J Mech Des 2004;127:788–98.
[17] Qingsong Xu, Yangmin Li, Ning Xi. Design, fabrication, and visual servo control of an XY parallel micromanipulator with piezo-actuation. IEEE Trans Automation Sci Eng 2009;6(October (4)).